Reprinted from

CMES

Computer Modeling in Engineering & Sciences

Founder and Editor-in-Chief:
Satya N. Atluri

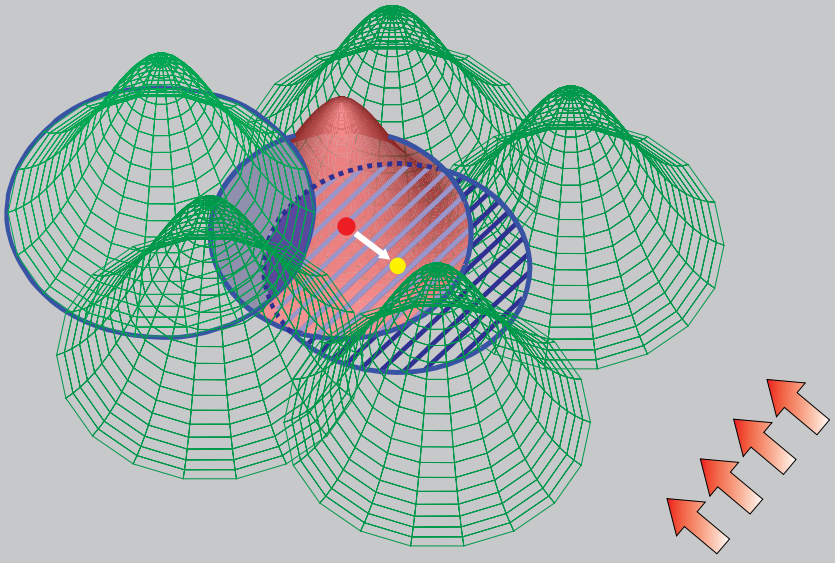

ISSN: 1526-1492 (print)
ISSN: 1526-1506 (on-line)

Tech Science Press

 CMES, vol.82, no.3, pp.195-213, 2011

Numerical Study of Dynamic Compression Process of Aluminum Foam with Material Point Method

Weiwei Gong [1], Xiong Zhang [1 2] and Xinming Qiu [1]

Abstract: Due to its high strength, low weight and strong anti impact capability, aluminum foam has great potential in the fields of transportation, aerospace and building structures as energy absorbing materials. Due to its complicated microstructures, it is desirable to develop an efficient numerical method to study the dynamic response of the aluminum foam under impact loading. In this paper, the material point method (MPM) is extended to the numerical simulation of the dynamic response of the aluminum foam under impact loading by incorporating the Deshpande Fleck's model and a volumetric strain failure model into our three-dimensional explicit material point method code, MPM3D. The developed method is first validated by comparing the numerical results obtained by MPM3D for a Taylor bar test with those obtained by LS-DYNA, and then is used to simulate the dynamic compression process of aluminum foam material. The numerical results show that the MPM has significant advantages in analyzing the high-speed dynamic characteristics of aluminum foam materials, and can be used in the practical applications of aluminum foam materials.

Keywords: Constitutive relations, aluminum foam, material point method, dynamic compression

1 Introduction

Aluminum foam is a type of aluminum based porous material with low weight, whose porosity is about $40\% \sim 90\%$. Aluminum foam has great advantages of high strength, low weight, strong anti impact capability and good noise abatement, making it an excellent energy-absorbing material.

A mass of research work indicates that there are three stages in the stress-strain curve compressing the aluminum foam: elastic region, plastic region and densification region as shown in Fig.1. The stress-strain curve of aluminum foam material

[1] School of Aerospace, Tsinghua University, Beijing 100084, P. R. China.
[2] Corresponding author: xzhang@tsinghua.edu.cn.

has a long platform, during which the plastic collapse occurs. A large amount of energy can be absorbed before reaching the compaction strain ε_D.

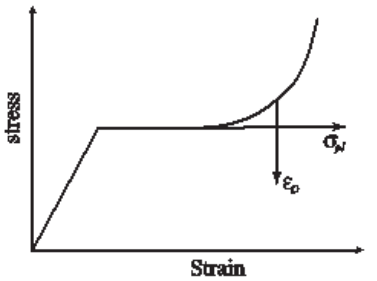

Figure 1: A classical stress-strain curve compressing aluminum foam

Many constitutive models have been developed for aluminum foam materials in the past decades. Gibson, Ashby, Zhang, and Triantafillou (1989) brought forward the first yield surface equation of the foam materials. Chen and Lu (2000) obtained the strain potential function of foam materials based on the assumption that the yield stress is the same during stretching or compressing. Bilkhu and Dubois established the constitutive model of foam materials based on the experiments of uniaxial and triaxial compressive tests [Hallquist (2006)]. Schreyer, Zuo, and Maji (1994) developed an anisotropy harden foam model. Besides these, there are plenty of constitutive models for foam materials, but some of them are too simple and some of them are too complicated with many unknown parameters. Most of them rarely involve the characteristics of random distribution of holes in porous materials and material failure.

Deshpande Fleck foam constitutive model (No. 154 material model in LS-DYNA) is a derivative model based on the classical Von Mises' yield criterion [Deshpande and Fleck (2000b)]. It has been widely applied in many engineering areas for its simple expression, good statistic property and convenience in adding different failure modes. For example, Hanssen, Girard, and Olovsson (2006) studied a bird strike problem using LS-DYNA, in which the protective shield made of aluminum foam is modeled by the Deshpande Fleck's model. Pinnoji, Mahajan, and Bourdet (2010) simulated the striking experiment of a motor helmet using the Deshpande Fleck's model for the aluminum foam inside.

With the developing of computer, the numerical methods have been widely used. In the Lagrangian finite element method (FEM), the mesh deforms with the material domain, so mesh distortion becomes serious in many problems, such as high velocity impact, explosion, and metal forming. In the Eulerian method, it is troublesome

to tack the material interfaces. Recently, the meshfree method has been developed and widely used in mechanics [Gu and Liu (2001); Gu and Zhang (2008); Gan, Chen, and Montgomery-Smith (2011); Rabczuk and Eibl (2006); Li and Liu (2002); Liu and Liu (2005)]. The meshfree method can avoid the mesh distortion because it uses the discrete points to construct trial functions. The material point method (MPM) as one of the classic meshfree method proposed by Sulsky, Chen, and Schreyer (1994) is an extension of the particle in cell method (PIC) [Harlow (1964); Brackbill, Kothe, and Ruppel (1988)] in computational fluid mechanics to solid mechanics, which combines the advantages of Lagrangian method and Eulerian method. In MPM, material domain is discretized by a set of material points (particles) that carry all state variables. The motion of these particles represents the motion and deformation of material. A background grid is used to solve the momentum equations and do spatial derivative calculation. Incorporation of constitutive models in MPM is relatively straightforward. In each time step, particles deform together with the gird nodes, so MPM avoids the difficulties associated with the material interfaces and mass flux between adjacent elements. In the next time step, the deformed grid is discarded and a new regular grid is used to avoid mesh distortion[Ma, Zhang, and Qiu (2009)]. Due to these characteristics, MPM has obvious advantages in modeling problems involving extreme large deformation, such as impact, contact, material damage and solid-fluid coupling problems.

In this paper, the Deshpande Fleck's model and a volumetric strain failure model are incorporated into our three-dimensional material point method code, MPM3D [Ma, Zhang, Lian, and Zhou (2009); Ma, Zhang, and Huang (2010); Zhang, Zhang, and Liu (2010)]. After validating MPM3D by comparing its numerical results for a Taylor bar test with those obtained by LS-DYNA, the dynamic process of compressing aluminum foam is further studied. The numerical results show that the MPM has significant advantages in analyzing the high-speed dynamic characteristics of aluminum foam materials.

2 Material Point Method

In the updated Lagrangian description, the current configuration is taken as the reference configuration. The weak form of the momentum equation is given by

$$\int_\Omega \rho \ddot{u}_i \delta u_i d\Omega + \int_\Omega \rho \sigma^s_{ij} \delta u_{i,j} d\Omega - \int_\Omega \rho f_i \delta u_i d\Omega - \int_{\Gamma_t} \rho \bar{t}^s_i \delta u_i d\Gamma = 0 \tag{1}$$

where $\sigma^s_{ij} = \sigma_{ij}/\rho$, $\bar{t}^s_i = \bar{t}_i/\rho$, σ_{ij} is the Cauchy stress tensor, $\bar{t}_i$ is the prescribed traction, and ρ is the density. $\ddot{u}_i$ is the acceleration, δu_i and $\delta u_{i,j}$ are the virtual displacement and its derivative, f_i is the body force.

Discretizing the continuum by a set of particles, the density ρ at any point x_i in the material domain can be approximated as

$$\rho(x_i) = \sum_{p=1}^{n_p} M_p \delta(x_i - x_{ip}) \tag{2}$$

where δ is the Dirac delta function, n_p is the total number of particles and x_{ip} are their coordinates.

In each time step, the particles are rigidly attached to the background grid, so the standard finite element shape function $N_I(x_i)$ of the grid can be used to map the information between the particles and the computational grid nodes. The variables with the subscript I are used to denote the variables belonging to the grid nodes, and the variables with the subscript p are used to denote the variables carried by the particles, namely $N_{Ip} = N_I(x_p)$. The value of a variable of the particle p, w_p, can be obtained by mapping its grid point values w_I to the particle using the standard finite element shape functions of the grid, namely

$$w_p = \sum_{I=1}^{n_g} N_{Ip} w_I \tag{3}$$

where n_g is the total number of grid nodes. If the eight-point hexahedron grid is used, the shape function of node I is given by

$$N_I = \frac{1}{8}(1+\xi\xi_I)(1+\eta\eta_I)(1+\varsigma\varsigma_I), I = 1,2,\cdots,8 \tag{4}$$

where ξ, η, ς are the natural coordinates which take values of ± 1 at the grid nodes. Substituting Eqs. (2) and (3) into the weak form (1), and invoking the arbitrariness of δu_{iI} yields

$$\dot{p}_{iI} = f_{iI}^{\text{int}} + f_{iI}^{\text{ext}}, \quad I = 1,2,\cdots,n_g \tag{5}$$

where

$$p_{iI} = m_I v_{iI} \tag{6}$$

is the momentum of grid node I if the lumped mass matrix is used,

$$f_{iI}^{\text{int}} = -\sum_{p=1}^{n_p} N_{Ip,j}\sigma_{ijp}\frac{m_p}{\rho_p} \tag{7}$$

$$f_{iI}^{\text{ext}} = \sum_{p=1}^{n_p} m_p N_{Ip} f_{ip} + \sum_{p=1}^{n_p} N_{Ip}\bar{t}_{ip}h^{-1}\frac{m_p}{\rho_p} \tag{8}$$

are the internal force and external force, respectively. In Eqs. (7) and (8), $\sigma_{ijp} = \sigma_{ij}(x_p)$, $f_{ip} = f_i(x_p)$.

The material points carry all the material information in MPM. In order to solve the momentum equations at time t^k on the computational grid, the mass and momentum of particle at time t^k need to be mapped to the computational grid nodes. After solving the momentum equations by the explicit integration algorithm, the increments in velocity and position of the grid nodes are mapped back to the particles to update their position and velocity. The particle stress can be updated by a constitutive model. There are three numerical schemes to update stress: the USL scheme, the MUSL scheme and the USF scheme[Bardenhagen (2002)]. In this paper, the MUSL scheme is used, so the updated particle momentum is mapped back to the computational grid again to calculate the nodal velocity

$$v_{iI}^{k+\frac{1}{2}} = \sum_{p=1}^{n_p} p_{ip}^{k+\frac{1}{2}} N_{Ip}^k / m_I^k \tag{9}$$

The incremental strain and vorticity are calculated from the nodal velocity to update the stress and density.

The central difference scheme is conditionally stable whose critical time step Δt_{cr} can be determined by

$$\Delta t_{\mathrm{cr}} = \min_e \frac{l_e}{c + |u|} \tag{10}$$

where l_e is the characteristic length of the cell e , u is the particle velocity,

$$c = \left[\frac{4G}{3\rho} + \left. \frac{\partial p}{\partial \rho} \right|_S \right]^{\frac{1}{2}}$$

is the sound speed of material and the subscript S denotes the isentropic process.

3 Constitutive model

The Deshpande Fleck foam model uses the hypoelastic-plasticity theory, which assumes that the elastic deformation is small enough compared with the plastic deformation. The rate-of-deformation tensor $\dot{\varepsilon}$ is divided into two parts as

$$\dot{\varepsilon}_{ij} = \dot{\varepsilon}_{ij}^e + \dot{\varepsilon}_{ij}^p \tag{11}$$

where superscripts e and p denote the elastic part and plastic part, respectively. The stress at time $t + dt$ can be obtained by integrating the stress rate as

$$\sigma_{ij}(t + dt) = \sigma_{ij}(t) + \dot{\sigma}_{ij} dt \tag{12}$$

The material derivative of Cauchy stress tensor $\dot{\sigma}_{ij}$ is not an objective tensor, so that the Jaumann rate of the Cauchy stress tensor

$$\sigma_{ij}^{\nabla} = \dot{\sigma}_{ij} - \sigma_{ik}\Omega_{jk} - \sigma_{jk}\Omega_{ik} \tag{13}$$

should be used in the constitutive equation [Belytchko, Liu, and Moran (2002)]. In Eq. (13), Ω_{jk} is the vorticity tensor.

The yield function Φ is defined as

$$\Phi = \hat{\sigma} - \sigma_y \leq 0 \tag{14}$$

where $\hat{\sigma}$ is the equivalent stress, which is expressed as

$$\hat{\sigma}^2 = \frac{\sigma_e^2 + \alpha^2\sigma_m^2}{1+(\alpha/3)^2} \tag{15}$$

in the Deshpande Fleck foam model [Deshpande and Fleck (2000b)], $\sigma_e = \sqrt{\frac{3}{2}\sigma'_{ij}\sigma'_{ij}}$ is the von Mises effective stress, $\sigma'_{ij} = \sigma_{ij} - \sigma_m\delta_{ij}$ is the deviatoric stress, $\sigma_m = \frac{1}{3}\sigma_{kk}$ is the mean stress, and

$$\alpha = \sqrt{\frac{9}{2}\frac{1-2\nu^p}{1+\nu^p}} \quad (0 \leq \alpha^2 \leq 4.5)$$

is the material parameter which controls the shape of the yield surface, where $\nu^p = -\dot{\varepsilon}_{11}^p/\dot{\varepsilon}_{33}^p$ is the plastic Poisson's ratio. When $\alpha^2 = 4.5$, $\nu^p = 0$, the uniaxial compression does not produce lateral plastic deformation. When $\alpha^2 = 0$, the yield criterion reduces to the von-Mises yield criterion [Reyes, Hopperstad, Berstad, and Langseth (2004)].

The plastic strain rate and equivalent strain rate are defined by the associated flow rule as

$$\dot{\varepsilon}_{ij}^p = \dot{\lambda}\frac{\partial\Phi}{\partial\sigma_{ij}} \tag{16}$$

$$\dot{\hat{\varepsilon}} = -\dot{\lambda}\frac{\partial\Phi}{\partial\sigma_y} = \dot{\lambda} \tag{17}$$

where $\dot{\lambda}$ is the plastic flow parameter. Loading and unloading conditions are given as

$$\dot{\lambda} \geq 0, \quad \Phi \leq 0, \quad \dot{\lambda}\Phi = 0 \tag{18}$$

It is shown that the elastic loading or unloading do not produce plastic flow ($\dot{\lambda} = 0$), and the stress state lies within the yield surface, i.e. $\Phi < 0$. In the case of plastic loading ($\dot{\lambda} > 0$), the stress state lies on the yield surface, i.e. $\Phi = 0$. The plastic strain rate is expressed as

$$\dot{\varepsilon}_{ij}^{p} = \dot{\lambda}\frac{\partial \Phi}{\partial \sigma_{ij}} = \dot{\hat{\varepsilon}}\frac{\partial \Phi}{\partial \sigma_e}\frac{\partial \sigma_e}{\partial \sigma_{ij}} + \dot{\hat{\varepsilon}}\frac{\partial \Phi}{\partial \sigma_m}\frac{\partial \sigma_m}{\partial \sigma_{ij}} \tag{19}$$

where

$$\frac{\partial \sigma_e}{\partial \sigma_{ij}} = \frac{3\sigma'_{ij}}{2\sigma_e} = n_{ij}, \quad \frac{\partial \sigma_m}{\partial \sigma_{ij}} = \frac{1}{3}\delta_{ij} \tag{20}$$

$$\frac{\partial \Phi}{\partial \sigma_e} = \frac{1}{1+(\alpha/3)^2}\frac{\sigma_e}{\hat{\sigma}}, \quad \frac{\partial \Phi}{\partial \sigma_m} = \frac{\alpha^2}{1+(\alpha/3)^2}\frac{\sigma_m}{\hat{\sigma}} \tag{21}$$

Substituting Eqs. (20) and (21) into Eq. (19) leads to

$$\dot{\varepsilon}_{ij}^{p} = \dot{\varepsilon}_e n_{ij} + \frac{1}{3}\dot{\varepsilon}_m \delta_{ij} \tag{22}$$

where

$$\dot{\varepsilon}_e = \sqrt{\frac{2}{3}\dot{\varepsilon}_{ij}^{\prime p}\dot{\varepsilon}_{ij}^{\prime p}} = \frac{\dot{\hat{\varepsilon}}}{1+(\alpha/3)^2}\frac{\sigma_e}{\hat{\sigma}} = \dot{\hat{\varepsilon}}\frac{\partial \Phi}{\partial \sigma_e} \tag{23}$$

is the von Mises effective plastic strain rate and

$$\dot{\varepsilon}_m = \dot{\varepsilon}_{kk}^{p} = \frac{\alpha^2\dot{\hat{\varepsilon}}}{1+(\alpha/3)^2}\frac{\sigma_m}{\hat{\sigma}} = \dot{\hat{\varepsilon}}\frac{\partial \Phi}{\partial \sigma_m} \tag{24}$$

is the volumetric plastic strain rate.

Upon substituting the expressions for σ_e and σ_m from Eqs. (23) and (24) into Eq. (15), the equivalent strain rate $\dot{\hat{\varepsilon}}$ can be expressed as

$$\dot{\hat{\varepsilon}}^2 = \left[1+\left(\frac{\alpha}{3}\right)^2\right]\left(\dot{\varepsilon}_e^2 + \frac{1}{\alpha^2}\dot{\varepsilon}_m^2\right) \tag{25}$$

Note that the equivalent strain rate $\dot{\hat{\varepsilon}}$ is the plastic work rate conjugate to the equivalent stress $\hat{\sigma}$, namely

$$\hat{\sigma}\dot{\hat{\varepsilon}} = \sigma_{ij}\dot{\varepsilon}_{ij}^{p} \tag{26}$$

The yield stress in the Deshpande Fleck foam model [Deshpande and Fleck (2000b)] is expressed as

$$\sigma_y = \sigma_p + \gamma \frac{\hat{\varepsilon}}{\varepsilon_D} + \alpha_2 \ln\left(\frac{1}{1-(\hat{\varepsilon}/\varepsilon_D)^\beta}\right) \tag{27}$$

where σ_p is the material parameter which denotes the initial yield strength, α_2, γ and β are the material parameters that are related to the density [Haanssen, Hopperstad, and Langseth (2002)],

$$\varepsilon_D = -\frac{9+\alpha^2}{3\alpha^2} \ln\left(\frac{\rho_f}{\rho_{f_0}}\right) \tag{28}$$

is the compaction strain. ρ_f denotes the foam density, ρ_{f_0} denotes the base material density.

4 Stress-update scheme

The purpose of the integration algorithm for the constitutive equation is, given the state variables σ_{ij}^n, ε_{ij}^{pn}, q_α^n at time t^n and strain increment $\Delta\varepsilon^{n+\frac{1}{2}} = \dot{\varepsilon}^{n+\frac{1}{2}} \Delta t^{n+\frac{1}{2}}$, to solve the state variables at time t^{n+1} that satisfy the loading-unloading conditions [Belytchko, Liu, and Moran (2002)]. Using the return mapping algorithm, it is assumed that the material is still in the elastic stage in the initial elastic-predictor step. The trial stress state $\sigma_{ij}^{*(n+1)}$ generally deviates from the yield surface at time t^{n+1}, therefore, a plastic-corrector step is required to return the stress state back to the updated yield surface. The trial elastic stress is given as

$$\sigma_{ij}^{*(n+1)} = \sigma_{ij}^n + (\sigma_{ik}^n \Omega_{jk}^{n+\frac{1}{2}} + \sigma_{jk}^n \Omega_{ik}^{n+\frac{1}{2}}) \Delta t^{n+1} + K \Delta\varepsilon_{kk}^{n+1} \delta_{ij} + 2G \Delta\varepsilon_{ij}^{\prime(n+1)} \tag{29}$$

The trial equivalent stress at time t^{n+1} is

$$\hat{\sigma}^{*(n+1)} = \sqrt{\frac{\left(\sigma_e^{*(n+1)}\right)^2 + \alpha^2 \left(\sigma_m^{*(n+1)}\right)^2}{1+(\alpha/3)^2}} \tag{30}$$

The trial yield function is

$$\Phi^{*(n+1)} = \hat{\sigma}^{*(n+1)} - Y\left(\hat{\varepsilon}^n\right) \tag{31}$$

which is a convex function. Plastic loading or unloading can be determined by the trial state. If $\Phi^{*(n+1)} < 0$, it indicates that the trial state is still elastic. There is no new plastic deformation produced during the process, so that the trial elastic

values are the real results. If $\Phi^{*(n+1)} > 0$, there will be a new plastic strain, so that a plastic-corrector step is needed to correct the trial stress state to satisfy the yield surface $\Phi(\sigma_{ij}^{n+1}, q_\alpha^{n+1}) = 0$.

In the plastic-corrector step, the corrected stress state can be obtained by subtracting the plastic correction $\Delta\sigma_{ij}^{n+1}$

$$\Delta\sigma_{ij}^{n+1} = K\Delta\varepsilon_m^{n+1}\delta_{ij} + 2G\Delta\varepsilon_e^{n+1}n_{ij}^{n+1} \tag{32}$$

from the trial stress $\sigma_{ij}^{*(n+1)}$ as

$$\sigma_m^{n+1} = \sigma_m^{*(n+1)} - K\Delta\hat{\varepsilon}_m^{n+1} = \frac{\sigma_m^{*(n+1)}}{1 + \frac{K\Delta\hat{\varepsilon}^{n+1}\alpha^2}{(1+(\alpha/3)^2)\hat{\sigma}^{n+1}}} \tag{33}$$

$$\sigma_e^{n+1} = \sigma_e^{*(n+1)} - 3G\Delta\hat{\varepsilon}_e^{n+1} = \frac{\sigma_e^{*(n+1)}}{1 + \frac{3G\Delta\hat{\varepsilon}^{n+1}}{(1+(\alpha/3)^2)\hat{\sigma}^{n+1}}} \tag{34}$$

In Eq. (32), $\Delta\varepsilon_m^{n+1}$ and $\Delta\varepsilon_e^{n+1}$ are the incremental volumetric plastic strain and von Mises effective plastic strain. According to Eqs. (23) and (24), we can get

$$\Delta\varepsilon_m^{n+1} = \Delta\hat{\varepsilon}^{n+1}\frac{\alpha^2}{1+(\alpha/3)^2}\frac{\sigma_m^{n+1}}{\hat{\sigma}^{n+1}} \tag{35}$$

$$\Delta\varepsilon_e^{n+1} = \Delta\hat{\varepsilon}^{n+1}\frac{1}{1+(\alpha/3)^2}\frac{\sigma_e^{n+1}}{\hat{\sigma}^{n+1}} \tag{36}$$

The stress update algorithm can be summarized as

1. Update the volume and density at $n+1$ step.
2. Calculate the trial stress $\sigma_{ij}^{*(n+1)}$, trial Mises effective stress $\sigma_e^{*(n+1)}$, and trial equivalent stress $\hat{\sigma}^{*(n+1)}$.
3. Calculate the trial yield function $\Phi^{*(n+1)}$ using Eq.(31), if $\Phi^{*(n+1)} \leq 0$, the trial state of elastic is the real state. Otherwise the following plastic-corrector step is needed to correct the trial stress state to satisfy the yield surface $\Phi^{(n+1)} = 0$.
4. The yield condition $\Phi^{n+1} = \hat{\sigma}^{n+1} - Y(\hat{\varepsilon}^{n+1}) = 0$ is a nonlinear equation about $\hat{\varepsilon}^{n+1}$ which can be solved using an iterative method. Let $\triangle\hat{\varepsilon}_k^{n+1}$ denote the k-th iteration step of $\triangle\hat{\varepsilon}^{n+1}$ and $\hat{\varepsilon}_k^{n+1}$ denote the k-th iteration step of $\hat{\varepsilon}^{n+1}$. The iteration process can be described as

(a) Initialization

$$k=0; \triangle\hat{\varepsilon}_{(0)}^{n+1}=0; \quad \hat{\varepsilon}_{(0)}^{n+1}=\hat{\varepsilon}^{n}; \quad \Phi_{(0)}^{n+1}=\hat{\sigma}^{*(n+1)}-Y^{n} \tag{37}$$

(b) Calculate

$$\left.\frac{\partial\Phi}{\partial\triangle\hat{\varepsilon}}\right|_{\triangle\hat{\varepsilon}=\triangle\hat{\varepsilon}_{k}^{n+1}}=\frac{\partial\Phi}{\partial\sigma_e}\frac{\partial\sigma_e}{\partial\triangle\hat{\varepsilon}}+\frac{\partial\Phi}{\partial\sigma_m}\frac{\partial\sigma_m}{\partial\triangle\hat{\varepsilon}}+\frac{\partial\Phi}{\partial\sigma_y}\frac{\partial\sigma_y}{\partial\triangle\hat{\varepsilon}} \tag{38}$$

$$\left.\frac{\partial Y}{\partial\hat{\varepsilon}}\right|_{\hat{\varepsilon}=\hat{\varepsilon}_{k}^{n+1}}=\frac{\gamma}{\varepsilon_D}+\frac{\alpha_2\beta(\frac{\hat{\varepsilon}}{\varepsilon_D})^{\beta-1}}{\varepsilon_D[1-(\frac{\hat{\varepsilon}}{\varepsilon_D})^{\beta}]} \tag{39}$$

(c) Update the effective plastic strain increment and the effective plastic strain

$$\triangle\hat{\varepsilon}_{(k+1)}^{n+1}=\triangle\hat{\varepsilon}_{k}^{n+1}-\frac{\Phi(\triangle\hat{\varepsilon}_{k}^{n+1})}{\left.\frac{\partial\Phi(\triangle\hat{\varepsilon})}{\partial\triangle\hat{\varepsilon}}\right|_{\triangle\hat{\varepsilon}=\triangle\hat{\varepsilon}_{k}^{n+1}}} \tag{40}$$

$$\hat{\varepsilon}_{(k+1)}^{n+1}=\hat{\varepsilon}^{n}+\triangle\hat{\varepsilon}_{(k+1)}^{n+1} \tag{41}$$

(d) update the yield stress

$$Y_{(k+1)}^{n+1}=Y^{n}+\left.\frac{\partial Y}{\partial\hat{\varepsilon}}\right|_{\hat{\varepsilon}=\hat{\varepsilon}_{(k+1)}^{n+1}}\triangle\hat{\varepsilon}_{(k+1)}^{n+1} \tag{42}$$

(e) Update the stress based on Eqs. (33) and (34) to update the stress. Calculate the corresponding Mises effective stress $\sigma_{e(k+1)}^{n+1}$, the effective stress $\hat{\sigma}_{(k+1)}^{n+1}$, and update the partial derivative of the function Φ with respect to the variable $\triangle\hat{\varepsilon}$

$$\left.\frac{\partial\Phi}{\partial\triangle\hat{\varepsilon}}\right|_{\triangle\hat{\varepsilon}=\triangle\hat{\varepsilon}_{(k+1)}^{n+1}}=\frac{\partial\Phi}{\partial\sigma_e}\frac{\partial\sigma_e}{\partial\triangle\hat{\varepsilon}}+\frac{\partial\Phi}{\partial\sigma_m}\frac{\partial\sigma_m}{\partial\triangle\hat{\varepsilon}}+\frac{\partial\Phi}{\partial\sigma_y}\frac{\partial\sigma_y}{\partial\triangle\hat{\varepsilon}} \tag{43}$$

(f) Calculate the current yield function $\Phi_{(k+1)}^{n+1}=\hat{\sigma}_{(k+1)}^{n+1}-Y_{(k+1)}^{n+1}$. If it is greater than the given tolerance value TOL, let $k=k+1$ and go to step 4c to continue the iteration. Otherwise, stop the iteration and take $\sigma_e^{n+1}=\sigma_{e(k+1)}^{n+1}$, $\hat{\sigma}^{n+1}=\hat{\sigma}_{(k+1)}^{n+1}$, $\triangle\hat{\varepsilon}^{n+1}=\triangle\hat{\varepsilon}_{(k+1)}^{n+1}$, $\hat{\varepsilon}^{n+1}=\hat{\varepsilon}_{(k+1)}^{n+1}$, $Y^{n+1}=Y_{(k+1)}^{n+1}$.

(g) Update the volumetric plastic strain $\triangle\varepsilon_m^{p(n+1)}$ and Mises effective plastic strain $\triangle\varepsilon_e^{p(n+1)}$ using Eqs. (35) and (36).

An important characteristic of metal foam is that the hydrostatic pressure will lead to changes in the bubble particles volume. When the volumetric strain reaches a certain value, the bubble particle will fail. The particle failure often occurs in the high-speed impact process, so a reasonable fracture criterion is needed. In this paper, a simple fracture criterion has been implemented in the constitutive model, in which the particle will fail when the volumetric strain ε_m reaches the critical strain $\varepsilon_{\mathrm{cr}}$ [Reyes, Hopperstad, Berstad, and Langseth (2004)].

Many researcheres have studied the shock wave propagation velocity, such as Lopatnikov, Gama, Haque, Krauthauser, Gillespie, and Guden (2003), Lopatnikov, Gama, Haque, Krauthauser, and Gillespie (2004) and Deshpande and Fleck (2000a). The effective wave speed of the metal foam in axial compression is expressed as

$$c = \sqrt{\frac{1}{\rho(\varepsilon,\rho_0)}} \frac{\partial \sigma(\varepsilon,\rho_0)}{\partial \varepsilon} \tag{44}$$

where $\sigma(\varepsilon,\rho_0)$ is the current axial stress, $\rho(\varepsilon,\rho_0) = \rho_0/(1-\varepsilon)$ is the current density, ρ_0 is the initial density, ε is the volumetric strain. In the elastic stage, the foam density is constant, but during the plastic stage, the hydrostatic pressure in the yield function will lead to changes in the particle volume, so the particle density will also change. In the compression process, the particle density is large and the wave speed is small, differing from the base material. With increasing the plastic strain, the metal foam will be almost completely compacted, so the effective wave speed of the foam is close to that of the base material.

5 Numerical examples

5.1 Taylor bar test

In order to validate the model and method, the Taylor bar problem is studied by using the commercial software LS-DYNA and MPM3D code. The length of the Taylor bar is 38.1 mm and its bottom radius is 12.7 mm. The total number of elements and nodes in FEM model are 17629 and 15360, respectively, whereas the number of particles in MPM model is 151680. The impact velocity is 100 m/s. The material constants of the Deshpande Fleck foam model are taken from Hanssen, Girard, and Olovsson (2006), and are listed in Tab.1.

Table 1: Material properties of the Deshpande Fleck foam model

ρ(kg/m^3)	E (MPa)	ν	α	γ(MPa)	ε_D	α_2(MPa)	β	σ_p(MPa)	$\varepsilon_{\mathrm{cr}}$
150	300	0.05	2.1	1.19	2.89	52.1	3.26	0.93	0.1

The time history of the kinetic and internal energy obtained by MPM3D and LS-DYNA are plotted in Fig.2, which shows that the kinetic energy and internal energy obtained by MPM3D are almost identical to that obtained by LS-DYNA. Furthermore, the deformations of the bar obtained by the two methods at 0.1 ms are in good agreement. The lengths of the bar obtained by the two methods are both changed from their original value of 38.1 mm to 29 mm, and the bottom radius are both changed from 12.7 mm to 14 mm.

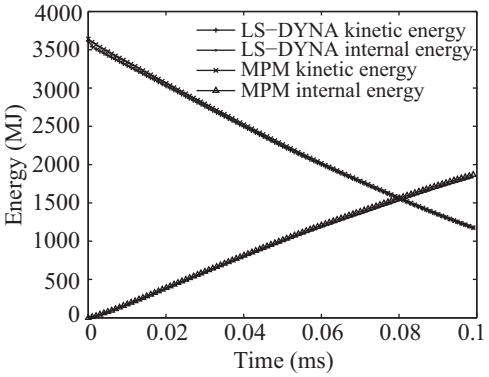

Figure 2: The time history of the kinetic and internal energy obtained by MPM3D and LS-DYNA

This test verify the constitutive model implemented in MPM3D, and it can be used to study the dynamic responses of the metal foam under impact loading.

5.2 Dynamic compression of aluminum foam

Aluminum foam has a long flat region in the stress-strain curve for absorbing energy, making it an excellent material for resisting impact. The dynamical properties of aluminum foam have to be determined by experiments in the practical applications. Because the experiments are usually very expensive, there is a desperate need for developing an efficient numerical simulation method. Here, the experiment conducted by Nemat-Nasser and Kang (2007) is simulated to further validate MPM3D. The experiment of Nemat-Nasser and Kang (2007) is similar to a simplified Hopkinson's pressure bar experiment for predicting the dynamical properties of materials. A simplified diagram of MPM model is shown in Fig.3. The bullet is a cylindrical 7075 aluminum bar with 78.2 mm in diameter, 114.3 mm in length and 1460 g in weight. The aluminum foam is made of aluminum 6101 and the relative density is $8\% \sim 10\%$. A 1/4 symmetric model is used for simulation. There is no friction between the bullet, output rod and the aluminum foam sample. The

nonreflecting boundary condition is used at the end of the output rod to inhibit the reflection of the elastic wave. The deformations of the bullet and output rod are small enough to be ignored in the experiment, thus the elastic model is used. The material properties of the bullet, output rod and aluminum foam are taken from Nemat-Nasser and Kang (2007) and are listed in Tab. 2.

Figure 3: MPM simulation model.

Table 2: Material properties used in the simulations of MPM3D

Materials	Density (kg/m^3)		Young (GPa)		Poisson	
Bullet	2770		70		0.345	
Output rod	7830		210		0.29	
Aluminum foam	Initial	Full compaction	Initial	Full compaction	Initial	Full compaction
	258	2770	0.054	70	0	0.345

The material properties of aluminum foam sample are obtained by fitting the stress-strain curve of the experiment in Nemat-Nasser and Kang (2007) and listed in Table3.

Table 3: The fitted material parameters of the aluminum foam

Yield Stress(MPa)	α	ε_D	α_2(MPa)	γ(MPa)	β
3	2.1	2.2	45	3.15	4

The aluminum foam sample used in the experiment of Nemat-Nasser and Kang (2007) has a very small Poisson's ratio. Even when the relative strain reaches 70%, the Poisson's ratio is only 0.08. Therefore, we assume that the Poisson's ratio equals zero in the simulation. Deshpande and Fleck (2000b) suggested that the Duocel aluminum foam is insensitive to the strain rate, thus the strain rate effect is also ignored here. Two experiments conducted in the reference are studied here, in which the initial velocities of bullet are 32.3 m/s and 52.6 m/s, respectively.

5.2.1 Experiment 1

Fig.4 compares the deformation of aluminum foam during compressing obtained by the experiment and MPM3D per 0.125 ms. Tab. 4 gives the measured and calculated length of aluminum foam sample during compressing, which shows that

the calculated results of MPM3D agree well with the experimental results. The final apparent strain reaches 58%.

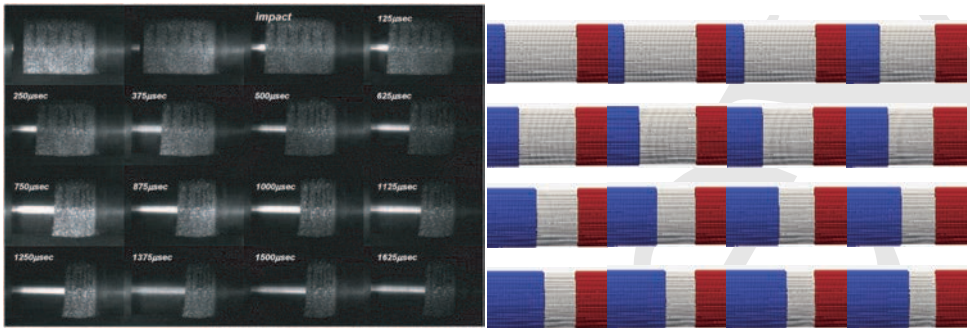

(a) Experiment (b) MPM3D

Figure 4: The deformation of aluminum foam during compressing obtained by the experiment and MPM3D when v=32.3 m/s.

Table 4: The measured and calculated length of aluminum foam sample per 0.125ms when v=32.3 m/s

time (ms)	0.0	0.125	0.25	0.375	0.5	0.625	0.75
experiment	76.2 mm	68.82 mm	63.9 mm	58.99 mm	54.07 mm	49.16 mm	44.24 mm
MPM	76.2 mm	68.82 mm	63.9 mm	60.22 mm	55.3 mm	50.38 mm	45.47 mm
time (ms)	0.875	1.0	1.125	1.25	1.375	1.5	1.625
experiment	41.78 mm	39.32 mm	36.87 mm	34.41 mm	33.92 mm	33.18 mm	31.95 mm
MPM	43.01 mm	40.55 mm	38.09 mm	35.64 mm	33.92 mm	33.18 mm	31.95 mm

To further validate MPM3D, this experiment is simulated by using MPM3D and LS-DYNA, respectively, and the time history of the engineering strain is compared. Three spots are selected along the aluminum foam sample: P3 at the front near the bullet, P2 in the middle and P1 at the end near the output rod. Fig.5 plots the time history of the engineering strain at spots P3, P2 and P1, respectively. Because of the time delay of the shock wave propagation in the aluminum foam, the deformation occurs at P3, P2 and P1 in succession. It is noted in the figures that although the deformations at P2 and P3 occur later than at P1, the strain increases more rapidly, leading to a steeper curve. The final maximum strains are 40% at P3, 60% at P2 and 70% at P1. The final strain distributes unevenly in the sample when v=32.3 m/s, because the stress wave reflected from the output rod will increase the total stress at P1.

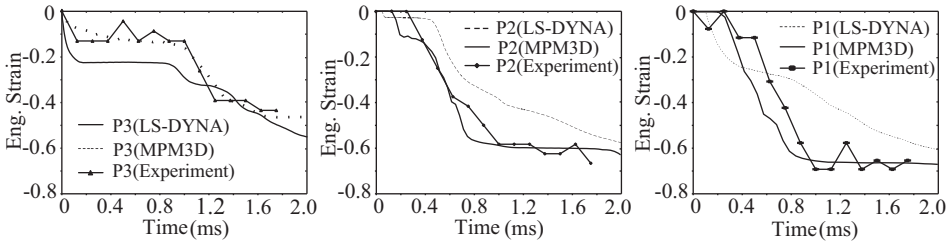

(a) P3 (b) P2 (c) P1

Figure 5: Time history of the engineering strain at spots P3, P2 and P1 of the sample when v=32.3m/s

5.2.2 Experiment 2

The initial velocity of the bullet in experiment 2 is 52.6 m/s. Fig.6 compares the deformation of the aluminum foam during compressing obtained by the experiment and MPM3D per 0.125 ms. Tab. 5 compares the measured and calculated length of aluminum foam sample during compressing, which shows that the simulation results of MPM3D agree well with the experimental results. The final strain of the sample is evenly 85%.

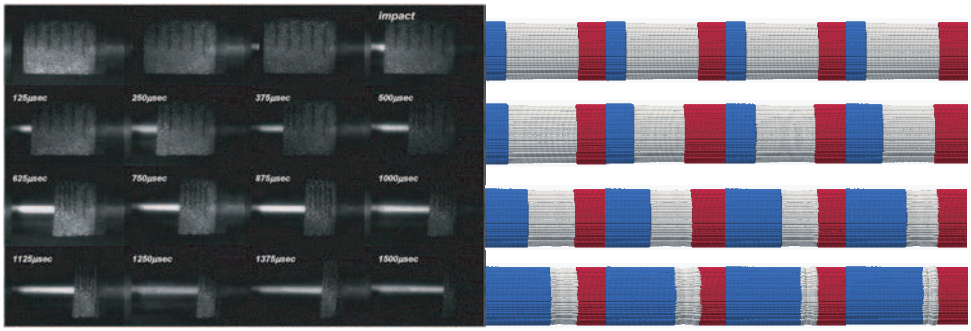

(a) Experiment (b) MPM3D

Figure 6: The deformation of aluminum foam during compressing obtained by the experiment and MPM3D when v=52.6 m/s

Similarly, Fig.7 plots the time history of the engineering strain at spots P3, P2 and P1 calculated from MPM3D and LS-DYNA. In all the simulation cases, MPM3D gives better agreement with the experimental results than LS-DYNA. It is noted in Fig.7 that the strain occurs first at P3, and then reaches 45% shortly. After that, the

Table 5: The measured and calculated length of aluminum foam sample per 0.125ms when v=52.6 m/s

time(ms)	0.0	0.125	0.25	0.375	0.5	0.625	0.75
experiment	76.2 mm	66.36 mm	61.45 mm	56.53 mm	49.16 mm	44.24 mm	36.87 mm
MPM	76.2 mm	66.36 mm	61.45 mm	56.53 mm	49.16 mm	44.24 mm	36.87 mm
time(ms)	0.875	1.0	1.125	1.25	1.375	1.5	
experiment	31.95 mm	29.49 mm	24.58 mm	19.66 mm	17.2 mm	14.74 mm	
MPM	31.95 mm	29.49 mm	24.58 mm	19.66 mm	17.2 mm	14.74 mm	

strain increases smoothly until about 0.1 ms. Finally the strain reaches about 85%. On the other hand, the strain at P1 occurs at 0.2 ms and increases smoothly. After about 0.8 ms, the strain increases drastically and reaches 85% in the end.

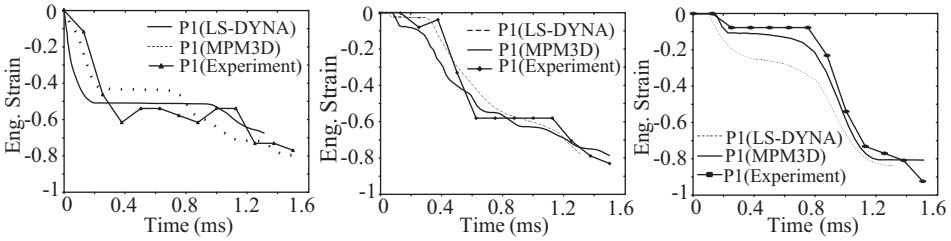

(a) P3 (b) P2 (c) P1

Figure 7: Time history of the engineering strain at spots P3, P2 and P1 of the sample when v=52.6 m/s

Compare the two cases of different initial velocities, the strains at different locations increase unevenly. The final strain remains uneven in the experiment 1 while the final strain comes to about 85% in the experiment 2. The uneven strain distribution in the sample is due to the large wave impedance in the output rod and bullet. The rise time of load pulse is shorter than the time needed to reach a stress balance. The aluminum foam sample cannot reach a uniform deformation before material failure.

The results obtained by MPM3D are closer to the experimental data than the results from LS-DYNA, showing the advantages of the MPM in solving the high-speed, large deformation problems. It should be noted that the efficient simulation time of LS-DYNA is only about 1.3 ms when the velocity is larger than 50 m/s, and then the mesh distortion will lead to the divergence and calculation failure. In contrast, MPM3D always give a reasonable result in high-speed cases. The deviation between the simulation result of MPM3D and experimental result may come from the deviation of the spatial position P1, P2 and P3. The aluminum foam in the

experiment is a typical porous material, but the constitutive model of MPM3D is a continuous model describing the macro-mechanical properties. The inaccurate model will also bring some deviation to the simulation.

6 Conclusions

We have incorporated the Deshpande Fleck foam constitutive model and volumetric strain failure modes into our 3D explicit MPM code, MPM3D. The complete iterative scheme for stress update is presented. The developed method is first validated by comparing the numerical result obtained by MPM3D for Taylor bar test with those obtained from LS-DYNA, and then used to simulate the dynamic compressing experiment of aluminum foam. The numerical results of MPM3D are closer to the experimental data from Nemat-Nasser and Kang (2007) than the results of LS-DYNA in all cases. Moreover, LS-DYNA fails in some cases because of the mesh distortion under high-speed conditions, while MPM3D can give reasonable results in all cases. It can be concluded that MPM is an efficient method for solving the large elastic-plastic deformation problems with high-speed impact.

Acknowledgement: This work was supported by the National Basic Research Program of China (2010CB832701) and National Natural Science Foundation of China (10872107).

References

Bardenhagen, S. G. (2002): Energy conservation error in the material point method for solid mechanics. *Journal of Computational Physics*, vol. 180(1), pp. 383–403.

Belytchko, T.; Liu, W. K.; Moran, B. (2002): *Nonlinear Finite Elements for Continua and Structures*. Wiley and Chichester.

Brackbill, J. U.; Kothe, D. B.; Ruppel, H. (1988): Flip: a low-dissipation, particle-in-cell method for fluid flow. *Computer Physics Communications*, vol. 48, pp. 25–38.

Chen, C.; Lu, T. J. (2000): A phenomenological framework of constitutive modeling for incompressible and compressible elasto-plastic solids. *International Journal of Solids and Structures*, vol. 37(52), pp. 7769–7786.

Deshpande, V. S.; Fleck, N. A. (2000): High strain rate compressive behavior of aluminium alloy foams. *International Journal of Impact Engineering*, vol. 24, pp. 277–298.

Deshpande, V. S.; Fleck, N. A. (2000): Isotropic constitutive models for metallic foams. *Journal of the Mechanics and Physics of Solids*, vol. 48(6-7), pp. 1253–1283.

Gan, Y.; Chen, C.; Montgomery-Smith, S. (2011): Improved material point method for simulating the zona failure response in piezo-assisted intracytoplasmic sperm injection. *CMES: Computer Modeling in Engineering & Sciences*, vol. 73(1), pp. 45–75.

Gibson, L. J.; Ashby, M. F.; Zhang, J.; Triantafillou, T. C. (1989): Failure surfacs for cellular materials under multi-axial loads-(i) modeling. *International Journal of Mechanical Sciences*, vol. 31(9), pp. 635–663.

Gu, Y. T.; Liu, G. R. (2001): A meshless local petrov-galerkin (mlpg) formulation for static and free vibration analyses of thin plates. *CMES: Computer Modeling in Engineering & Sciences*, vol. 2(4), pp. 463–476.

Gu, Y. T.; Zhang, L. C. (2008): Coupling of the meshfree and finite element methods for determination of the crack tip fields. *Engineering Fracture Mechanics*, vol. 75, pp. 986–1004.

Haanssen, A. G.; Hopperstad, O. S.; Langseth, M. (2002): Validation of constitutive models applicable to aluminium foams. *International Journal of Mechanical Sciences*, vol. 44, pp. 359–406.

Hallquist, J. O. (2006): *LS-DYNA theory manual*. Livermore Software Technology Corporation, 7374 Las Positas Road. Livermore, California 94551, 2006.

Hanssen, A. G.; Girard, Y.; Olovsson, L. (2006): A numerical model for bird strike of aluminium foam-based sandwich panels. *International Journal of Impact Engineering*, vol. 32, pp. 1127–1144.

Harlow, F. H. (1964): The particle-in-cell computing method for fluid dynamics. *Methods in Computational Physics*, vol. 3, pp. 319–345.

Li, S.; Liu, W. K. (2002): Meshfree and particle methods and their applications. *Applied Mechanics Reviews*, vol. 55(1), pp. 1Â¨C34.

Liu, X.; Liu, G. R. (2005): Radial point interpolation collocation method for the solution of nonlinear poisson problems. *Computational Mechanics*, vol. 36(4), pp. 298Â¨C306.

Lopatnikov, S. L.; Gama, B. A.; Haque, M. J.; Krauthauser, C.; Gillespie, J. W. (2004): High-velocity plate impact of metal foams. *International Journal of Impact Engineering*, vol. 30, pp. 421–445.

Lopatnikov, S. L.; Gama, B. A.; Haque, M. J.; Krauthauser, C.; Gillespie, J. W.; Guden, M. (2003): Dynamics of metal foam deformation during taylor

cylinder-hopkinson bar impact experiment. *Composite Structures*, vol. 61, pp. 61–71.

Ma, S.; Zhang, X.; Lian, Y. P.; Zhou, X. (2009): Simulation of high explosive explosion using adaptive material point method. *CMES: Computer Modeling in Engineering & Sciences*, vol. 39, no. 2, pp. 101–123.

Ma, S.; Zhang, X.; Qiu, X. M. (2009): Comparison study of mpm and sph in modeling hypervelocity impact problems. *International Journal of Impact Engineering*, vol. 36, pp. 272–282.

Ma, Z. T.; Zhang, X.; Huang, P. (2010): An object-oriented mpm framework for simulation of large deformation and contact of numerous grains. *CMES: Computer Modeling in Engineering & Sciences*, vol. 55, no. 1, pp. 61–88.

Nemat-Nasser, S.; Kang, W. J. (2007): Experimental investigation of energy-absorption characteristics of components of sandwich structures. *International Journal of Impact Engineering*, vol. 34, pp. 1119–1146.

Pinnoji, P. K.; Mahajan, P.; Bourdet, N. (2010): Impact dynamics of metal foam shells for motorcycle helmets: Experiments & numerical modeling. *International Journal of Impact Engineering*, vol. 37, pp. 274–284.

Rabczuk, T.; Eibl, J. (2006): Modelling dynamic failure of concrete with meshfree methods. *International Journal of Impact Engineering*, vol. 32(11), pp. 1878–1897.

Reyes, A.; Hopperstad, O. S.; Berstad, T.; Langseth, M. (2004): Implementation of a constitutive model for aluminum foam including fracture and statistical variation of density. In *8th International LS-DYNA Users Conference*.

Schreyer, H. L.; Zuo, Q. H.; Maji, A. K. (1994): Anisotropic plasticity model for foams and honeycombs. *Journal of Engineering Mechanics*, vol. 120(9), pp. 1913–1930.

Sulsky, D.; Chen, Z.; Schreyer, H. L. (1994): A particle method for history-dependent materials. *Computer Methods in Applied Mechanics and Engineering*, vol. 118(1-2), pp. 179–196.

Zhang, Y. T.; Zhang, X.; Liu, Y. (2010): An alternated grid updating parallel algorithm for material point method using openmp. *CMES: Computer Modeling in Engineering & Sciences*, vol. 69, no. 2, pp. 143–165.

CMES: Computer Modeling in Engineering & Sciences

ISSN : 1526-1492 (Print); 1526-1506 (Online)

Journal website:
http://www.techscience.com/cmes/

Manuscript submission
http://submission.techscience.com

Published by
Tech Science Press
5805 State Bridge Rd, Suite G108
Duluth, GA 30097-8220, USA

Phone (+1) 678-392-3292
Fax (+1) 678-922-2259
Email: sale@techscience.com
Website: http://www.techscience.com
Subscription: http://order.techscience.com

CMES is Indexed & Abstracted in
Applied Mechanics Reviews; Cambridge Scientific Abstracts (Aerospace and High Technology; Materials Sciences & Engineering; and Computer & Information Systems Abstracts Database); CompuMath Citation Index; Current Contents: Engineering, Computing & Technology; Engineering Index (Compendex); INSPEC Databases; Mathematical Reviews; MathSci Net; Mechanics; Science Alert; Science Citation Index; Science Navigator; Zentralblatt fur Mathematik.